Results in Engineering 22 (2024) 102145

Contents lists available at ScienceDirect

Results in Engineering

journal homepage: www.sciencedirect.com/journal/results-in-engineering

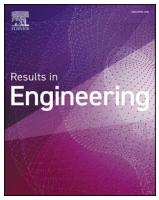

Assessing the influence of aneurysm dimensions on hemodynamic patterns and wall deformation dynamics for predicting rupture risk

Ermia Azari Moghaddam [a], Aisa Rassoli [b], Hossein Darvish [c], Nasser Fatouraee [a,*]

[a] Biological Fluid Dynamics Laboratory, The Amir Kabir University of Technology, Tehran, Iran
[b] Department of Mechanical Engineering, K.N. Toosi University of Technology, Tehran, Iran
[c] University of Salento, Lecce, Italy

ARTICLE INFO

Keywords:
Fluid-structure interaction
Cerebral aneurysms
Rupture prediction
Hemodynamic factors

ABSTRACT

Cerebral aneurysms are among the most dangerous cardiovascular diseases which display no symptoms prior to reaching critical conditions. As cerebral aneurysms are deadly diseases with a very small treatment window after reaching the critical stage, numerical investigations of this phenomenon are commonly used to assess the risk of rupture. In this study, the fluid-structure interaction (FSI) method is used to analyze the effects of aneurysm size on hemodynamic factors predicting rupture in three aneurysms of different geometries, at the same location, and using the same boundary conditions. In the present study, the aneurysms experience TAWSS at values under 2 Pa in incremented areas as the aneurysmal sizes increase, this is while the relatively larger distribution of high TAWSS (as high as 20 Pa) regions are perceived in smaller aneurysms. Furthermore, the maximum OSI stands at below 0.05 in the smaller cases while the larger case experiences a maximum OSI as high as 0.2, which is considered a predictive parameter for rupture. The vortex core lines experience discontinuities with increased aneurysmal size, which is in agreement with the development of flow complexities with size. The hemodynamics factors such as the time-averaged wall shear stress (TAWSS), oscillatory shear index (OSI), and vortex core line investigated in this study, suggest that greater size can be considered a major risk factor for rupture. In addition to that, we have found that the displacement trend of the aneurysm changes as size increases; developing more in the dome rather than the aneurysmal sac. This change in trend might also present a potential to be used as a predictive parameter.

1. Introduction

An aneurysm is an arterial anomaly caused by the weakening and dilation of a part of a blood vessel [1]. Although the pathogenesis of aneurysms remains in the dark, the growing consensus of the reason for this pathogenesis is the gradual degeneration of media and the elastin fibers within this layer [2]. One of the common locations for the occurrence of an aneurysm is in the cerebral artery network; hence known as a cerebral aneurysm [3]. The prevalence of cerebral aneurysms has been reported to stand at a mean value of 1–5 % worldwide [3], and the prevalence of subarachnoidal hemorrhage (SaH) has been reported to range from 2 to 22 patients in a population of 100000 persons, on a yearly basis [4]. While the incidences are infrequent, elevated risk of post-rupture strokes and further complications are significant and a 30-day mortality risk of 45 % has been reported in SaH survivors [5]. Furthermore, it is reported that an estimated 30 % of the SaH survivors experience moderate-to-severe disabilities [5]. Post-treatment complications such as recurrence, cerebrospinal fluid leakage, and ischemic complications have also been reported in review studies [6–8]. Considering the highly invasive nature of medical interventions and possible post-intervention complications, it is best to avoid unnecessary interventions. In order to avoid such interventions, it is crucial to study and predict aneurysmal rupture.

It is known that the hemodynamics of an aneurysm play a crucial role in the progression and eventual rupture of the aneurysm [9]. Furthermore, the mechanical properties of the vascular wall also affect the fate of an aneurysm [10]. Considering the fact that the critical stage in aneurysms presents a small window for interventions, in-vivo studies in human patients are not a possible feat. This is why in-vitro and in-silico studies are generally available in this field. The in-silico studies include CFD, FSI, and AI-based approaches to study the phenomenon behind the

* Corresponding author. Biological Fluid Mechanics Research Laboratory, Faculty of Biomedical Engineering, Amirkabir University of Technology (Tehran Polytechnic), Tehran, P.O. Box: 15875, I.R. Iran, 15914.
E-mail address: nasser@aut.ac.ir (N. Fatouraee).

https://doi.org/10.1016/j.rineng.2024.102145
Received 21 February 2024; Received in revised form 6 April 2024; Accepted 15 April 2024
Available online 20 April 2024

Nomenclature

CFD	Computational Fluid Dynamics
OSI	Oscillatory Shear Index
TAWSS	Time-Averaged Wall Shear Stress
ρ^f	Fluid density
v^f	Fluid velocity
p	Pressure
f^b	Body force
t	Time
μ	Dynamic viscosity
τ^s	Solid stress
d_f	Fluid grid displacement
I_2	Second invariant of the Cauchy-Green strain tensor
n	Normal vector
FSI	Fluid-Structure Interaction
SaH	Subarachnoidal Hemorrhage
WSS	Wall Shear Stress
ρ^s	Solid density
w^f	Fluid grid velocity
τ^f	Fluid stress
v	Velocity
I	Unit tensor
e^f	Velocity strain tensor
d^s	Solid displacement
I_1	First invariant of the Cauchy-Green strain tensor
C_{ab}	Mooney-Rivlin coefficients

rupture, interventions, and their risks. In the CFD approach, the wall properties are neglected and only the hemodynamic indices are investigated [11–14], while FSI studies also include the effects of the mechanical properties of the wall on the hemodynamic indices, as well as the aneurysm [15–18].

Retrospective studies point out hemodynamic indices that help predict the chances of aneurysmal rupture. Hemodynamic indices such as WSS, TAWSS, OSI, as well as flow complexity, have been proven to have predictive results concerning cerebral aneurysms. Although there are controversies regarding some indices [19], the generally accepted parameters are relatively clear. The WSS is the most controversial hemodynamic parameter used in the field of cerebral aneurysms. Although it is relatively clear that high WSS is generally responsible for the initiation of aneurysms [20,21], low WSS in the aneurysmal area is reported to be effective in the prediction of rupture [22]. It is shown that low WSS in the aneurysmal region triggers a mechanoreceptor reaction that leads to the degeneration of the wall, which in turn leads to rupture [23]. While there are myriad applications of computational studies in the field of cerebral aneurysms, the present study focuses on rupture prediction and the hemodynamic factors associated with it. Although WSS has been shown to exhibit different ranges of magnitudes, up to an approximate value of 250 pa [24], the distribution is generally low on the aneurysmal region [25], and the neck region of the aneurysm is generally prone to higher distributions of WSS. While lower WSS signifies a more immediate risk of rupture, elevated WSS and TAWSS can potentially lead to the growth of secondary blebs [26] and even multiple aneurysms [27], which in turn intensify the risk of rupture. It is established that the distribution and magnitude of WSS are highly affected by the boundary conditions and the geometry; the aneurysm, the location, and the mother vessel [23]. Hypertension modeled as elevated pressure at boundaries has been exhibited to increase the distribution of not only the WSS [28] but also the solid displacement in FSI studies [17]; the latter experiencing greater effects. The flow characteristics are also another predicting parameter regarding aneurysmal rupture. The general flow inside an aneurysm is laminar and experiences vortexes towards the downstream of the flow [29]; however, flow complexities also happen in some aneurysms, contributing to the rupture prediction. The most inclusive classification of aneurysmal flows is presented by Cebral et al. [30], classifying the aneurysmal flows into 3 types and 2 classes for each type; the flow complexity (simple and complex flow), inflow type (concentrated and diffuse inflow); and impingement zones (small and large impingements). While each class comes with its unique series of possible complications, the complex flow is presented as a rupture predictor. The presence of blebs is also an indicator of complicated flow patterns, which in turn indicate a higher risk of rupture [26]. Although most aneurysms present simple flow patterns [27], the flow complexity and pattern are highly affected by the aneurysm geometry, location, and mother vessel; similar to the WSS. This also suggests possible relations between the flow pattern and the WSS. This suggestion is verified by Adib et al. [31], who concluded that the WSS is not only dependent on the boundary conditions but also the inflow conditions. The OSI is the index shedding light on the direction alternation of the wall shear stress, with zero signifying a fully unidirectional flow, and 0.5 signifying a fully alternating flow. The OSI is also considered a rupture predictor. It is also an index to predict other medical complications, such as atherosclerosis and intraluminal thrombosis [21]. This index generally displays very low values (~0) in human vessels, and an OSI magnitude as low as 0.1 can be considered relatively high and risky [32–34]. All the hemodynamic parameters discussed, generally offer a relatively accurate prediction for the rupture of a target aneurysm. It is known that CFD generally overestimates the WSS distribution in comparison to FSI studies [35], thus causing possible errors in the low WSS rupture predictor. This overestimation is especially increased in higher blood pressures, pointing at the possible weakness of the CFD method in the prediction of rupture in cases with hypertension.

While CFD studies present good predictive capabilities, the overestimations in the WSS distributions are generally countered by FSI studies. It is also suggested that CFD studies not only overestimate the WSS but also the flow velocity, which is more evident in higher pressure conditions [35]. The drawback of FSI studies is the introduction of a new set of equations which increase the computational costs significantly, which is why FSI studies are less frequently conducted. FSI studies have investigated the effects of the aneurysmal wall thickness [15], coupling schemes [16], solid properties [18,36], and boundary conditions [15,28,35] on the hemodynamic indices, as well as solid displacements. Other studies have also investigated the risks of post-operational complications [37], as well as intervention planning for surgical alternatives [38].

The present study addresses the fluid-solid interaction analysis of three different aneurysms, placed on a mother vessel of the middle cerebral artery bifurcation. Previous studies are either based on ideal geometries or patient-specific cases of aneurysms. This study helps to offer insight into the effects of size indices on the same mother vessel and under the same boundary conditions and to assess the independent effect of aneurysm size on predictive indices, which are the main parameters considered by surgeons for interventions. The boundary conditions are extracted from a flow-validated, anatomical model of a Circle of Willis with 10 boundary conditions, increasing the accuracy of the boundary conditions in comparison to the conventional Womersley profile inlet. While retrospective studies have emphasized the sensitivity of computational analyses regarding the boundary conditions [39,40], there has not been a study utilizing a verified boundary condition of an entire Circle of Willis. The present investigation also introduces an additional predictive parameter that could prove to be useful in the

Table 1
Specifications of the modeled aneurysms.

Case number	Maximum diameter (mm)	Height (mm)	Aspect ratio
1	1.7	2.5	1.2
2	2.5	3.6	1.3
3	2.7	5.8	1.6

prediction of aneurysmal rupture.

2. Methods and materials

2.1. Geometry

The geometry used in this study was obtained by truncation and editing of a patient-specific circle of Willis, extracted in a previous study by the same team, and the whole geometry generation has been presented in the same study [41]. In order to analyze the aneurysms under similar conditions, we have used the boundary conditions and geometry obtained by the mentioned study. Mesh editing software MeshMixer was used to add an aneurysmal region to the intact vessel, and also create the solid volume for the fluid-solid interaction analysis. The geometries of the aneurysms were created based on statistical data presented by other studies to create models closer to real anatomical models [42]. Table 1 presents the specifications of the aneurysm geometries and Fig. 1 displays the obtained geometries.

2.2. Mathematical formulations

2.2.1. Fluid formulation

Blood being a suspension consisting of plasma and hematocytes, displays Non-Newtonian behavior in lower shear rates. The high shear rate nature of this flow allows us to approximate blood properties as a Newtonian fluid with a density of 1050 kg/m^3 and a viscosity of 0.004 Pa s. Blood flow in non-aorta arteries can be assumed laminar, as the Reynolds number does not exceed several hundred [43], and the present study is no exception (Re < 600). Considering the pulsatile nature of the boundary conditions as presented in our previous study [41], the continuity equation (equation (1)), and the Navier-Stokes equations (equation (2)) are solved by considering transient flow, hence including the variable time.

$$\rho^f\left(\frac{\partial p}{\partial t}+\left(v^f-w^f\right).\nabla p\right)+\rho_m\nabla.v^f=0 \tag{1}$$

$$\rho^f\left(\frac{\partial v}{\partial t}+\left(v^f-w^f\right).\nabla v^f\right)-\nabla.\tau^f=f^b \tag{2}$$

Where ρ^f depicts the fluid density, v^f depicts the fluid velocity, w^f depicts the fluid grid velocity, p depicts the hydrostatic pressure, τ^f depicts the fluid stress, f^B depicts body forces, and ∇ is the gradient operator. While fluid problems are investigated in the Eulerian frame and solid problems are addressed in the Lagrangian frame, the subtraction of the grid velocity from the fluid velocity in the momentum equation, enables us to use the Arbitrary Lagrangian-Eulerian (ALE) method to solve for the fluid-solid interaction. This allows the fluid domain to directly accommodate the effect of solid displacement on the fluid domain, while exerting fluid pressure on the solid domain.

The stress tensor in the Navier-Stokes equation is shown below:

$$\tau^f=-pI+2\mu e^f \tag{3}$$

Where I denotes the second-order unit tensor, μ denotes the dynamic viscosity, and e^f indicates the velocity strain tensor.

2.2.2. Solid formulation

Lagrangian solid is defined as:

$$\frac{\partial\tau^s}{\partial x}=\rho^s\frac{\partial^2 d^s}{\partial t^2} \tag{4}$$

Where τ^s is the stress, ρ^s the density, and d^s the displacement in the solid domain.

The Mooney-Rivlin hyperelastic model was used to model the solid domain as it is known to be one of the most accurate models for living tissue [16]. The Mooney-Rivlin hyperelastic model describes the solid behavior using the strain energy. The governing equation for a 5-parameter Mooney-Rivlin hyperelastic material is given as follows:

$$W=C_{10}(I_1-3)+C_{01}(I_2-3)+C_{11}(I_1-3)(I_2-3)+C_{20}(I_1-3)^2+C_{02}(I_2-3)^2 \tag{5}$$

where W is the strain energy function, I_1 and I_2 are the first and second invariants of the Cauchy-Green strain tensor, and C_{ab} are the experimental coefficients. The coefficients were obtained from a study by Valencia et al. [16], and are presented in Table 2. These properties were associated with the aneurysmal region to study its solid displacement and effect on the fluid pattern and other parameters of the region.

Table 2
Mooney-Rivlin parameters.

Row	Coefficient	Value (MPa)
1	C_{10}	0.3848
2	C_{01}	−0.0891
3	C_{11}	0.5118
4	C_{20}	0.5109
5	C_{02}	0.4912

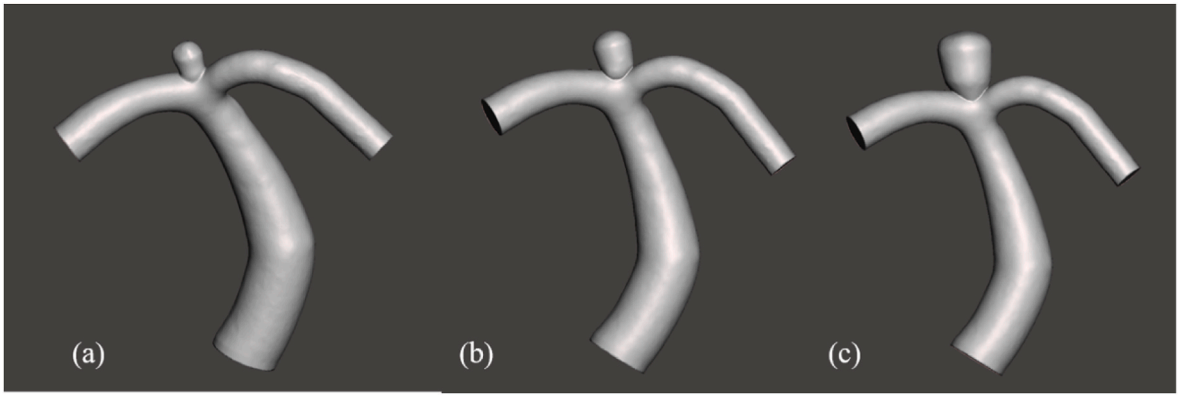

Fig. 1. The three cases used in this study: (a) case one, (b) case two, and (c) case three.

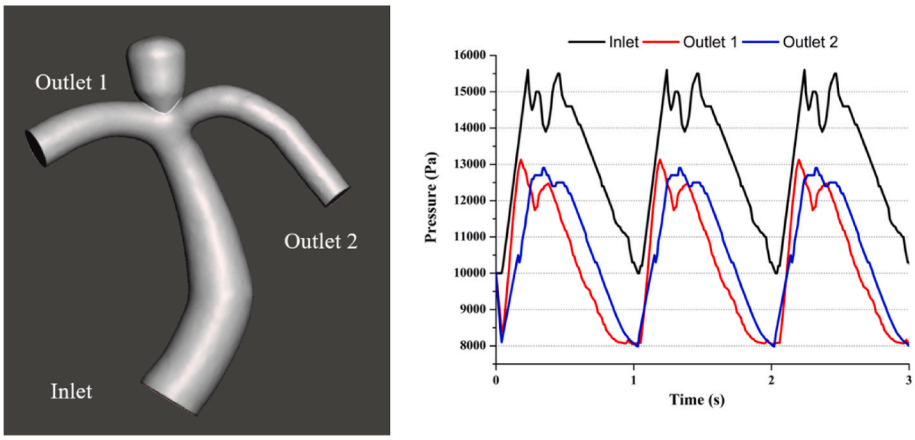

Fig. 2. The boundaries' locations and conditions.

2.2.3. Fluid-solid interaction

The fluid-solid interaction enables the solution of both the fluid and the solid domains while coupling the stresses and displacements to study the effect of either domain on the other. In this case, the fluid stresses are applied as boundary conditions to the solid, and the resultant solid domain displacement causes a deformation in the fluid domain. The fluid-solid interface is the surface at which the two domains meet. It is hence, crucial to ensure the compatibility of the two domains. In this study, the compatibility equations are defined as the dynamic and the kinematic conditions.

The kinematic compatibility equation is defined as:

$$d_f = d_s \tag{6}$$

coupling the displacement of the mutual interface. The letter "d" depicts the displacement, and the subscripts "f" and "s" depict the fluid and the solid domains, respectively. This coupling enables the movement of the fluid grid, hence introducing the term "w" in equations (1) and (2).

The dynamic compatibility equation is defined as:

$$(\sigma.n)_{fluid} = (\sigma.n)_{solid} \tag{7}$$

coupling the stresses at the mutual interface. This coupling enables the interface to include the effects of stresses by one domain to be felt by the other as well. As mentioned earlier, solid mechanics is generally solved in the Lagrangian system, while fluid mechanics is addressed by the Eulerian frame. However, when the fluid-solid interactions are of importance, the fluid domain must be solved using the Arbitrary Lagrangian-Eulerian formulation to enable the coupling of the two domains.

2.3. Boundary conditions

The boundary conditions used in the present study were obtained from a previous study by the same research team [41]. The effect of stroke on the flow rates of boundaries of a complete circle of Willis was analyzed in the aforementioned study. In order to reduce the computational cost, we have reduced the geometry to a single middle cerebral artery bifurcation and aneurysms. The boundary conditions for the entire circle of Willis were used to re-create the results from the previous study, and the pressure at the sections (turning into the present study boundaries) was extracted and used as the input to the present study; hence, validating the model and the conditions. The boundary conditions are given in Fig. 2.

The solid-mechanics structure has three distinct boundary conditions. The base of the wall has been fixed to the mother artery, and the surface in direct contact with the fluid has the Fluid-Structure Interface condition which follows the compatibility equations presented in the previous section. The rest of the solid boundaries are free boundaries to allow deformation under the effects of the fluid stress.

2.4. Numerical details

The simulations were performed by using ADINA 9.7. ADINA uses a finite-element method to discretize and solve both the solid mechanics and the fluid flow model simultaneously through an ALE formulation as explained in the previous sections. The two-way fluid-structure coupling scheme was used to solve the model, applying the solid displacement on the fluid nodes through the ALE formulation, and the fluid pressure on the solid domain. The sparse matrix was solved with a maximum of 1000 iterations for the fluid domain and 150 iterations for the fluid-structure interaction. The time step was set to 0.005 s, spanning over 3 simultaneous cycles. The mesh-independency was also performed using a mesh density scale in order to accommodate all models. The final mesh density requirement was found to be 2500 elements per cubic millimeter. A sample of the meshed geometry is displayed in Fig. 3. It is noteworthy that temperature effects, gravitational effects, and the intracranial pressure are neglected to reduce computational costs.

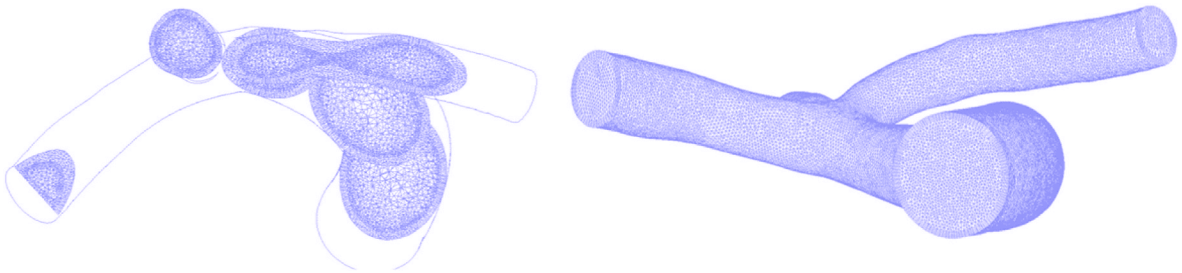

Fig. 3. Sample of the created mesh.

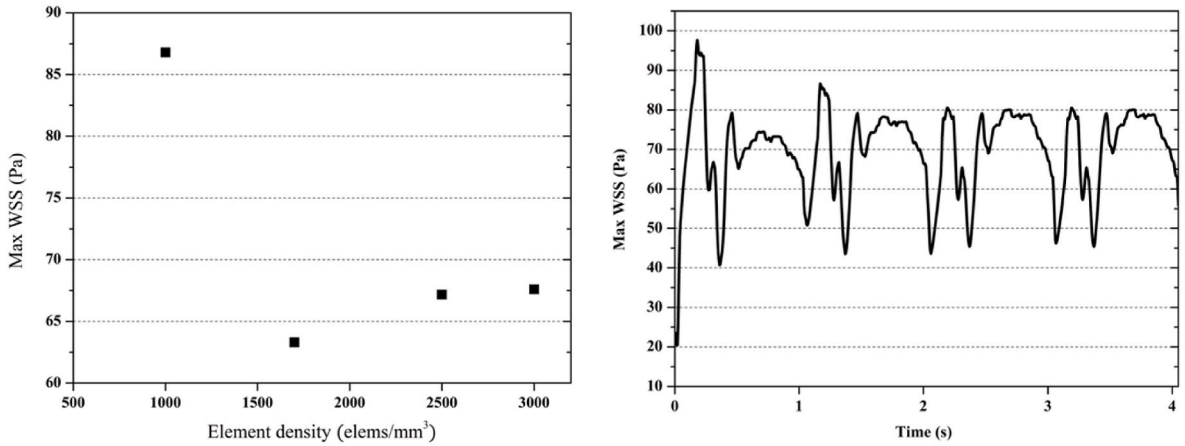

Fig. 4. Grid convergence and cycle independency analyses results.

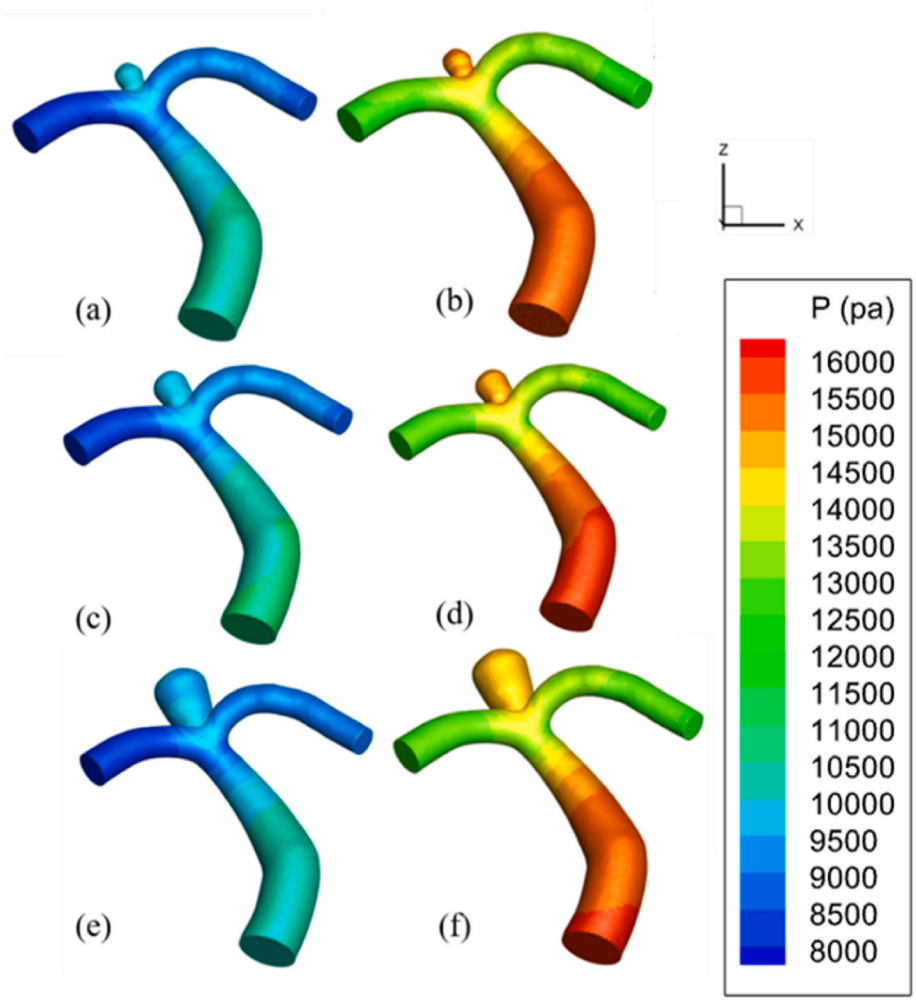

Fig. 5. The pressure distribution contours for model numbers (a) & (b) one, (c) & (d) two, and (e) & (f) three, during the diastolic (contours on the left) and the systolic phases (contours on the right).

3. Results and discussion

3.1. Mesh convergence and cycle independence analysis

To ensure the accuracy of the simulations, as well as the elimination of the initial values, mesh convergence and cycle independence were analyzed. In order for the mesh convergence to be applicable to all cases, the maximum WSS was investigated as mesh density in 4 different densities. The results indicate that for densities 2500 elements/mm^3 and above, the errors are below 5 %, which indicate that the results are independent of the mesh density. In addition, the simulations spanned over 4 cycles to ensure the independence from the initial values, which

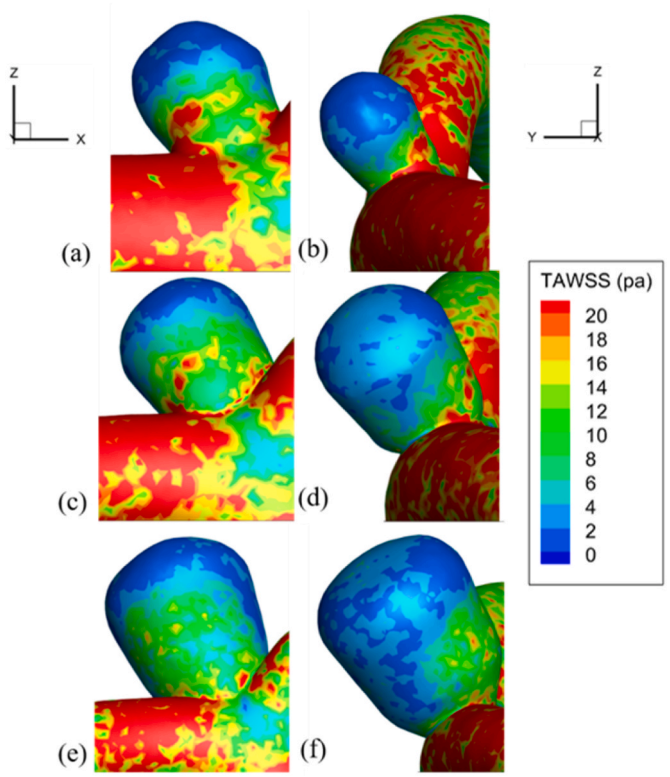

Fig. 6. TAWSS distribution on the model numbers (a) & (b) one, (c) & (d) two, and (e) & (f) three.

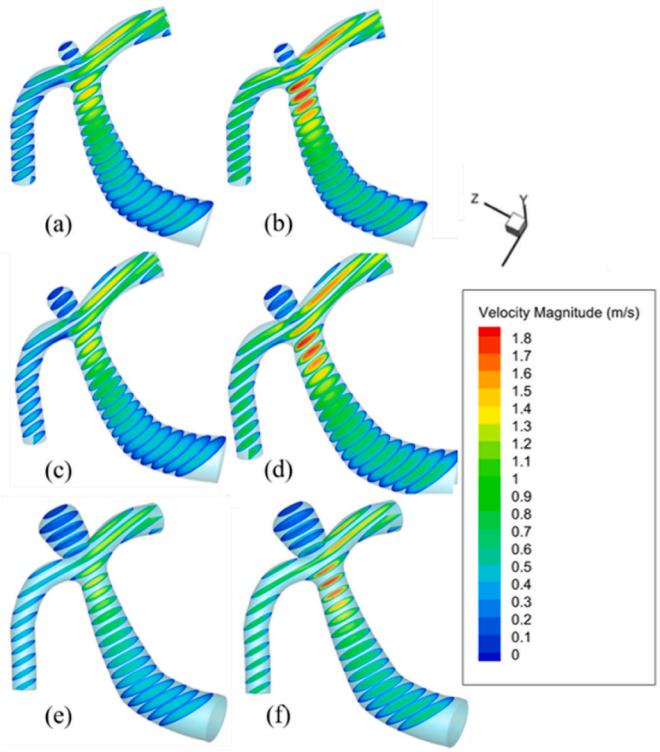

Fig. 7. The velocity distribution contours for model numbers (a) & (b) one, (c) & (d) two, and (e) & (f) three, during the diastolic (contours on the left) and the systolic phases (contours on the right).

conclude that the results from the third cycle onwards display minimal error, thus proving cycle independence at cycle 3. The mentioned investigations are displayed in Fig. 4.

3.2. Pressure distribution

As mentioned earlier, the boundary conditions used for the models are the same and hence, the pressure distribution is only affected by the aneurysm geometry, which is relatively negligible. The distribution contours can be seen in Fig. 5. As evident, the aneurysm sac experiences an accumulation of pressure which decreases with size, and the rest of the vessel experiences approximately the same distribution of pressure. The pressure elevation at the aneurysmal sac is shown to exert a negligible effect on the rupture risk of aneurysms [44]. Although it has recently been suggested that the pressure inside an aneurysm sac can predict areas of higher risk for thin-wall formation, this would require further investigations to be a reliable hemodynamic index [14].

3.3. Shear stress

One of the hemodynamic indices used in the analysis of cerebral aneurysms is the wall shear stress. Fig. 6 displays the time-averaged wall shear stress (TAWSS) of the three models in two distinct views (XZ and YZ planes). Considering the lower magnitudes of WSS on the aneurysmal sac, the band has been adjusted to avoid the WSS on the vessel overshadowing the aneurysmal sac. The neck region of the aneurysmal sacs hosts the greatest WSS distribution, and the distribution decays, moving towards the tip of the dome. It is evident that the TAWSS distribution decays as the aneurysm size increases, suggesting that greater sizes encourage lower WSS distribution. It is also noteworthy that larger aneurysms lead to negligibly lower WSS distribution on the mother vessel. Similar results are reported by Shojima et al. [25], who suggested that higher WSS either occurs in the mother vessel or the aneurysmal neck.

It is established that higher WSS is effective in the initiation of aneurysms, and low WSS distributions lead to rupture in the long-term [22]. Zhang et al. [45] presented the incidence of very low WSS values on the rupture points, while the magnitude and region of high WSS were shown to be irrelevant in rupture prediction. Chronic low WSS in the aneurysmal sac triggers mechanoreceptor responses that lead to the degeneration and weakening of the aneurysmal wall which culminates in the rupture of the aneurysm [25].

Fukazawa et al. [46] reported that very low WSS was seen in the rupture point of aneurysms, while the WSS distribution on the aneurysmal sac could be larger than the mother vessel. Despite the relationship between the WSS and rupture risk, the study does not report a relationship between geometrical indices such as size and aspect ratio with the rupture risk, which is in controversy with similar studies. The present study also displays very low WSS on the aneurysmal region; especially the dome. It is also perceivable that larger aneurysms accommodate larger areas with low WSS distribution which could also be used as a rupture predictor [47], suggesting an increased risk of rupture with larger aneurysm sizes.

3.4. Velocity distribution

Fig. 7 displays the velocity distribution within the three models during the diastolic and systolic phases. As evident, the velocity distribution within the aneurysmal region is lower in comparison to the mother vessel; hence, a more detailed look into the flow within the aneurysmal region could shed light on the behavior of velocity in this region. Fig. 8 displays the velocity distribution within the aneurysmal region of the three models. The velocity distribution within the aneurysmal sacs reveals that greater neck size results in greater velocity distribution and greater aneurysm size results in a thinner layer of stagnant blood. This layer becomes thinner during the systolic phase and accumulates thickness during the diastolic phase. This is while lower velocities can be seen in the middle of larger aneurysms, suggesting stagnant flow in that region. It can be perceived that as the aneurysm

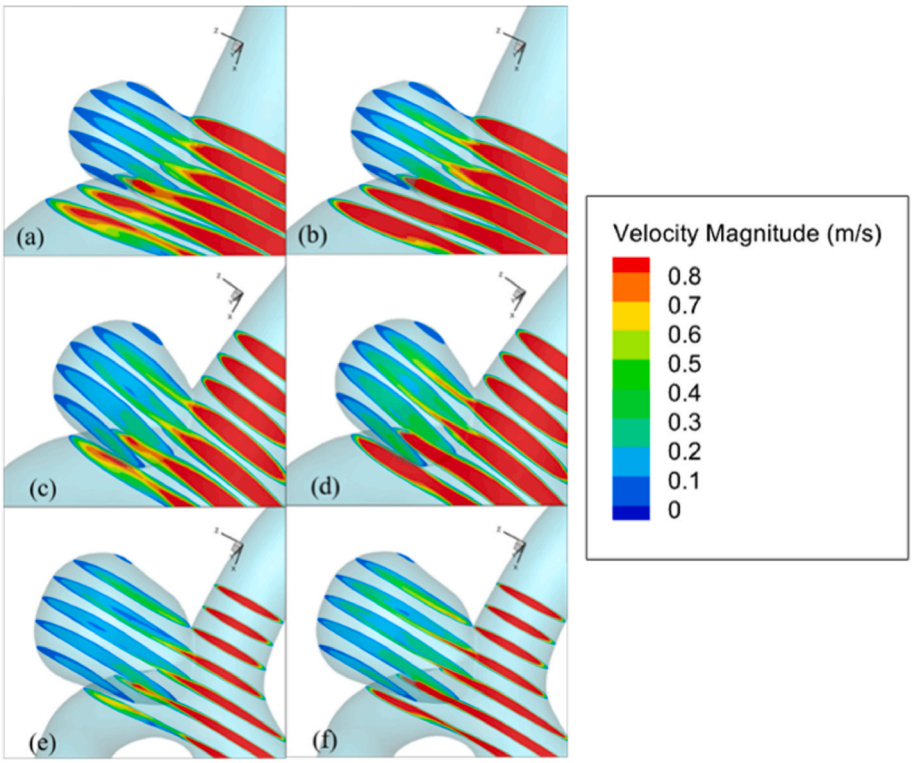

Fig. 8. The velocity distribution contours within aneurysms for model numbers (a) & (b) one, (c) & (d) two, and (e) & (f) three, during the diastolic (contours on the left) and the systolic phases (contours on the right).

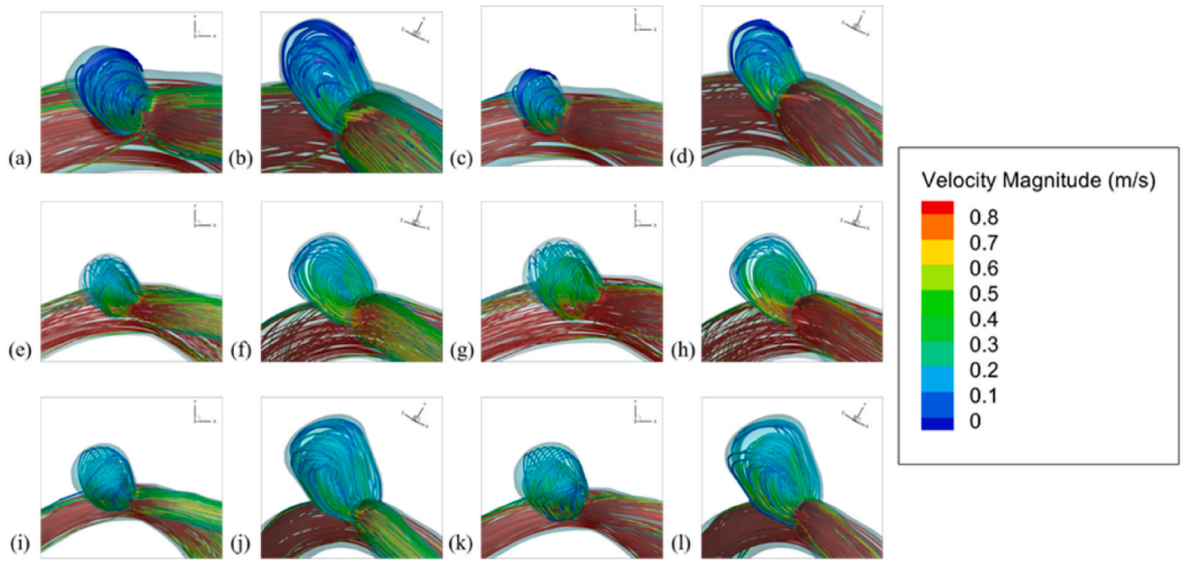

Fig. 9. Streamlines within the aneurysmal region for model numbers one (first row), two (second row), and three (third row), during the diastolic (first and second columns) and the systolic (third and fourth columns) phases.

size increases, the stagnant layer thickness in close proximity with the decays, and reappears in the middle region of the aneurysm.

3.5. Flow complexity

The streamlines serve as a presentation of the flow complexity within the aneurysms. The streamlines are presented in Fig. 9. As evident in Fig. 9 (a)–(d), the flow inside the first model is a relatively simple flow with one vortex. It is also perceivable that the flow pattern experiences a negligible change during the diastolic phase in comparison to the systolic phase. This is while the second model experiences a higher velocity and a more complex flow pattern as depicted by Fig. 9 (e)–(h). As evident in Fig. 9 (f) & (h), flow complexity develops in the second model, and is also a recipient of the effect of time; changing flow pattern to a negligible extent, however greater than in model number one. Model number three, however, experiences the most complex flow inside the aneurysmal sac. This is evident in Fig. 9 (i)–(l). In model number three not only does the velocity change with time, but also the pattern undergoes evident changes. The streamlines are displayed in multiple directions, suggesting the complexity of flow within the third model.

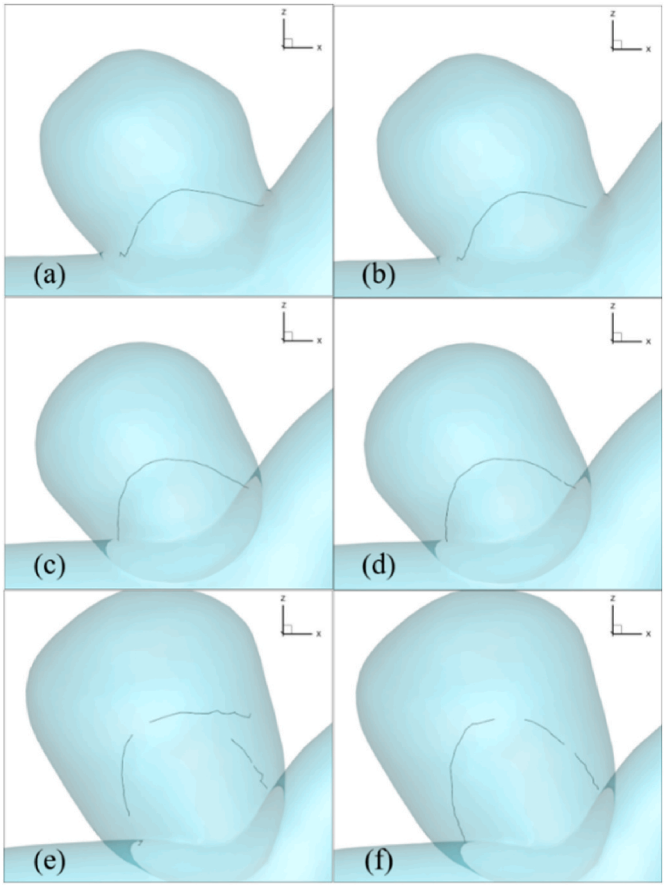

Fig. 10. The vortex core lines for model numbers (a) & (b) one, (c) & (d) two, and (e) & (f) three, during the diastolic (contours on the left) and the systolic phases (contours on the right).

While the streamlines are a depiction of the flow complexity, the investigation of the vortex core lines also proves to be insightful to the analysis of flow complexity. The vortex core lines trace the cores of vortices within the flow and join them as a line. Fig. 10 displays the vortex core lines in the three models. Fig. 10 (a)–(d) suggest that with an increase in aneurysm size, the vortex core line also reaches higher heights in the aneurysmal region. Although this does not necessarily depict a more complex flow within a larger aneurysm, the streamlines do suggest such an event. Fig. 10 (e) & (f) display the vortex core lines in model number three. As evident, the vortex core lines are discontinuous at multiple points, and the core line pattern also changes while moving from the systolic phase to the diastolic phase, suggesting a complex flow that also changes with time.

The flow pattern within an aneurysm can be different and unique; however, it is established that most cerebral aneurysms experience a single vortex in the sac. While the mentioned fact is perceived in most cases, the complexity of flow serves as a rupture predictor. Complex flows, hosting two or more vortices are reported as a predictor for aneurysmal rupture [30]. The flow pattern is also shown to be effective in the distribution of the WSS. Shojima et al. [25] reported an increased WSS especially in the neck, in aneurysms with the simple flow patterns. This is while aneurysms with a more complex flow display a lower WSS distribution on the sac, which is also regarded in the present study. This would suggest that the flow complexity, being a rupture predictor by itself, is also effective on WSS which is also a rupture predictor. The vortex core line length is also reported to be a predictive parameter in the rupture of cerebral aneurysms. It is reported that longer vortex core lines are more common in aneurysms with a higher risk of rupture [48]. The present study displays flow disturbances with increased aneurysm size. While model one presents a simple flow pattern, the flow develops into more complex patterns as the aneurysm size increases. The vortex core line also experiences a similar fate with size. It is also evident that discontinuity occurs only in the largest model, hinting at possible correlations between vortex core line discontinuity and rupture risk of aneurysms.

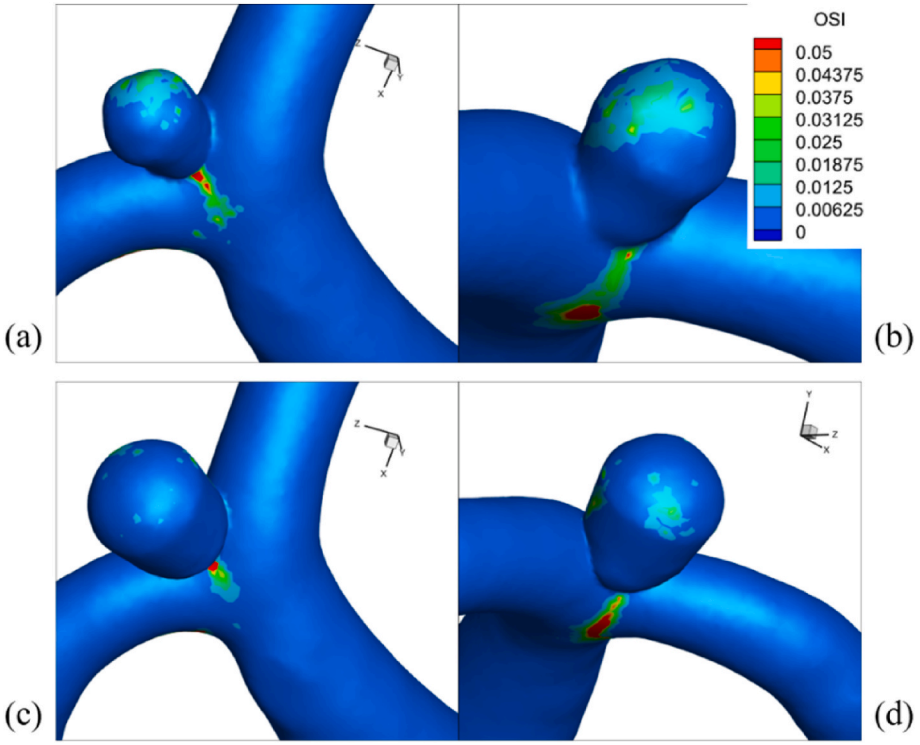

Fig. 11. The Oscillatory Shear Index for model numbers (a) & (b) one, and (c) & (d) two in two distinct views.

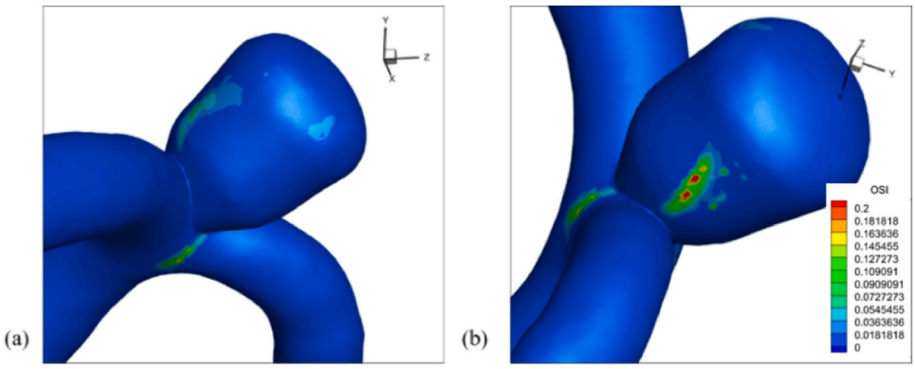

Fig. 12. The Oscillatory Shear Index for model number three in two distinct views.

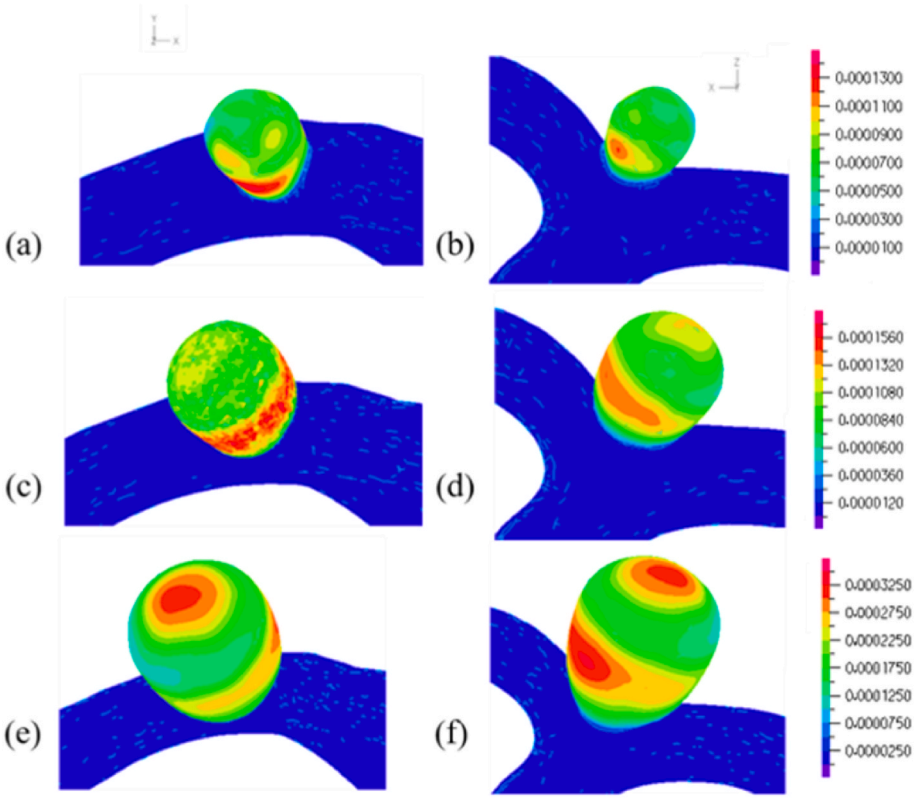

Fig. 13. The solid displacement contours for model numbers (a) & (b) one, (c) & (d) two, and (e) & (f) three in two distinct views (Values are given in mm).

3.6. Oscillatory shear index (OSI)

The OSI is an index that signifies the alternating nature of flow. This value ranges from zero to 0.5 with zero depicting a fully simple, single-directional flow, and 0.5 depicting a fully alternating flow. This index is generally employed to predict secondary complications, such as thrombosis in aneurysms. It is established that the OSI is relatively low in the human vessels; generally ranging below 0.1.

As evident in Figs. 11 and 12, the OSI distribution experiences a peak in all models on the neck of the aneurysm in the direction of the mother vessel. While the OSI in models one and two experiences a maximum value of approximately 0.05, occurring on the neck, the third model experiences a maximum of approximately 0.2, which is a relatively high OSI, which also appears on the aneurysmal sac of the model.

It is known that low WSS coupled with a high OSI could supply the baseline for secondary medical complications such as arterial atherosclerosis and thrombosis [21]. Although Zhang et al. [45] report the OSI to be a non-independent parameter, it is established that high OSI coupled with low WSS is a relatively accurate predictor for aneurysmal rupture [33]. The relatively high OSI of 0.2 in the third model of the present study suggests that the third aneurysm experiences sudden changes in the flow direction, which is also perceived from the streamlines and vortex core lines, further verifying the complex flow observation in the third model. Hence, the third model experiences the higher risk of rupture regarding the OSI.

3.7. Solid displacement

The final parameter that will be presented is the solid displacement. The solid displacement is a result of the FSI simulation, and cannot be presented via conventional CFD studies. As evident in Fig. 13 (a) & (b), the highest displacement in the first model occurs in the circumference of the aneurysmal sac, and the value peaks at 0.14 mm. This is while Fig. 13 (c) & (d) display the displacement contour for the second model,

displaying a development of a high displacement region in the tip of the dome. As evident, the circumference of the aneurysmal sac still experiences a high displacement, while the tip of the dome starts to display higher displacements in comparison to the first model. The displacement in the second model also peaks at 0.16 mm. Finally, the third model as depicted by Fig. 13 (e) & (f) displays a greater displacement in the tip of the aneurysmal sac. The high displacement region on the tip of the dome has developed in the third model, peaking at 0.33 mm. Interestingly, a study by Lee et al. [18] presented a similar pattern for displacement, where the unruptured aneurysms generally experienced a higher displacement in the neck and sac region, while the ruptured aneurysms exhibit higher nodal displacements towards the dome of the aneurysm.

It is known that 84 % of ruptured aneurysms experience rupture at the tip of the aneurysmal dome [49]. While this fact is not supportive enough to conclude that the solid displacement trend serves as a rupture predictor, the critical condition of the hemodynamic factors influencing the models, coupled with the solid displacement trend in the third model suggests a possible correlation between the displacement trend and risk of rupture.

4. Conclusions

The present study investigates the effects of aneurysm geometry, especially size, on multiple hemodynamic parameters. The fluid-structure interaction method was employed to simulate the complex phenomenon. The findings of the present study conclude.

- A model has been extracted with the boundary conditions from an entire Circle of Willis, ensuring a more physiologically accurate model
- FSI modeling was used to predict WSS, TAWSS, and flow conditions with better accuracy than conventional CFD
- WSS and TAWSS experience a decaying trend with increased aneurysmal size, increasing the risk of rupture
- The solid displacement trend varies with aneurysm size, exhibiting higher displacements at the dome with increased aneurysmal size
- The vortex core lines present the changes in the trend of vortices within the aneurysmal region, which can be used together with flow complications to predict the risk of rupture

The limitations of this study include the numeric nature of in-silico studies giving rise to minor errors and simplifying assumptions. Newtonian behavior assumption for blood is another simplifying assumption that was made to reduce computational costs. On the other hand, the utilization of the boundary conditions from an entire Circle of Willis can be considered as the major novelty of the present study.

It is worth mentioning that the effects of vortex core lines are still far from understood and could be the focus of prospective investigations. Furthermore, the displacement trend and magnitude would also require more attention and research to fully understand the correlation with rupture risk. In addition, the investigation of larger networks for instance an entire Circle of Willis with aneurysms could also offer insight into the effects of distal vessels and multiple aneurysms on rupture risks.

CRediT authorship contribution statement

Ermia Azari Moghaddam: Writing – original draft, Software, Methodology, Investigation, Formal analysis. **Aisa Rassoli:** Writing – review & editing, Software, Methodology. **Hossein Darvish:** Software, Investigation. **Nasser Fatouraee:** Writing – review & editing, Supervision.

Declaration of competing interest

The authors declare that they have no known competing financial interests or personal relationships that could have appeared to influence the work reported in this paper.

Data availability

Data will be made available on request.

References

[1] Inc., A. D. A. . (n.d.) Aneurysm. Retrieved October 25, 2022, from https://medlineplus.gov/ency/article/001122.htm.

[2] J.D. Humphrey, C.A. Taylor, Intracranial and abdominal aortic aneurysms: similarities, differences, and need for a new class of computational models, Annu. Rev. Biomed. Eng. 10 (1) (2008) 221–246, https://doi.org/10.1146/annurev.bioeng.10.061807.160439.

[3] J.L. Brisman, J.K. Song, D.W. Newell, Cerebral aneurysms, N. Engl. J. Med. 355 (9) (2006) 928–939, https://doi.org/10.1056/NEJMra052760.

[4] V.L. Feigin, C.M. Lawes, D.A. Bennett, S.L. Barker-Collo, V. Parag, Worldwide stroke incidence and early case fatality reported in 56 population-based studies: a systematic review, Lancet Neurol. 8 (4) (2009) 355–369, https://doi.org/10.1016/S1474-4422(09)70025-0.

[5] S.C. Johnston, S. Selvin, D.R. Gress, The burden, trends, and demographics of mortality from subarachnoid hemorrhage, Neurology 50 (5) (1998) 1413–1418, https://doi.org/10.1212/WNL.50.5.1413.

[6] R. Martinez-Perez, D.A. Hardesty, G. Silveira-Bertazzo, T. Albonette-Felicio, R. L. Carrau, D.M. Prevedello, Safety and effectiveness of endoscopic endonasal intracranial aneurysm clipping: a systematic review, Neurosurg. Rev. 44 (2) (2021) 889–896, https://doi.org/10.1007/s10143-020-01316-0.

[7] B.M. Kim, Y.S. Shin, S.-H. Kim, S.H. Suh, Y.-K. Ihn, D.I. Kim, S. Il Park, Incidence and risk factors of recurrence after endovascular treatment of intracranial vertebrobasilar dissecting aneurysms, Stroke 42 (9) (2011) 2425–2430, https://doi.org/10.1161/STROKEAHA.111.617381.

[8] S. Bsat, A. Bsat, H. Tamim, H. Chanbour, S.O. Alomari, M. N. El Houshiemy, I. Omeis, Safety of stent-assisted coiling for the treatment of wide-necked ruptured aneurysm: a systematic literature review and meta-analysis of prevalence, Intervent Neuroradiol. 26 (5) (2020) 547–556, https://doi.org/10.1177/1591019920945059.

[9] M. Shojima, M. Oshima, K. Takagi, R. Torii, M. Hayakawa, K. Katada, T. Kirino, Magnitude and role of wall shear stress on cerebral aneurysm, Stroke 35 (11) (2004) 2500–2505, https://doi.org/10.1161/01.STR.0000144648.89172.0f.

[10] M. Couade, M. Pernot, C. Prada, E. Messas, J. Emmerich, P. Bruneval, M. Tanter, Quantitative assessment of arterial wall biomechanical properties using shear wave imaging, Ultrasound Med. Biol. 36 (10) (2010) 1662–1676, https://doi.org/10.1016/j.ultrasmedbio.2010.07.004.

[11] A. Sarrami-Foroushani, M.-C. Villa-Uriol, M. Nasr Esfahany, S.C. Coley, L.Y. Di Marco, A.F. Frangi, A. Marzo, Modeling of the acute effects of primary hypertension and hypotension on the hemodynamics of intracranial aneurysms, Ann. Biomed. Eng. 43 (1) (2015) 207–221, https://doi.org/10.1007/s10439-014-1076-7.

[12] A.Y.-S. Tang, W.-C. Chung, E.T.-Y. Liu, J.-Q. Qu, A.C.-O. Tsang, G.K.-K. Leung, K.-W. Chow, Computational fluid dynamics study of bifurcation aneurysms treated with pipeline embolization device: side branch diameter study, J. Med. Biol. Eng. 35 (3) (2015) 293–304, https://doi.org/10.1007/s40846-015-0046-3.

[13] J.H. Kim, H. Han, Y.-J. Moon, S. Suh, T.-H. Kwon, J.H. Kim, W.-K. Yoon, Hemodynamic features of microsurgically identified, thin-walled regions of unruptured middle cerebral artery aneurysms characterized using computational fluid dynamics, Neurosurgery 86 (6) (2020) 851–859, https://doi.org/10.1093/neuros/nyz311.

[14] H. Kimura, S. Osaki, K. Hayashi, M. Taniguchi, Y. Fujita, T. Seta, E. Kohmura, Newly identified hemodynamic parameter to predict thin-walled regions of unruptured cerebral aneurysms using computational fluid dynamics analysis, World Neurosurgery 152 (2021) e377–e386, https://doi.org/10.1016/j.wneu.2021.05.107.

[15] H.T. Sun, K.Y. Sze, A.Y.S. Tang, A.C.O. Tsang, A.C.H. Yu, K.W. Chow, Effects of aspect ratio, wall thickness and hypertension in the patient-specific computational modeling of cerebral aneurysms using fluid-structure interaction analysis, Engineering Applications of Computational Fluid Mechanics 13 (1) (2019) 229–244, https://doi.org/10.1080/19942060.2019.1572540.

[16] A. Valencia, P. Burdiles, M. Ignat, J. Mura, E. Bravo, R. Rivera, J. Sordo, Fluid structural analysis of human cerebral aneurysm using their own wall mechanical properties, Comput. Math. Methods Med. (2013) 1–18, https://doi.org/10.1155/2013/293128, 2013.

[17] A. Valencia, F. Torres, Effects of hypertension and pressure gradient in a human cerebral aneurysm using fluid structure interaction simulations, J. Mech. Med. Biol. 17 (1) (2017) 1750018, https://doi.org/10.1142/S021951941750018X.

[18] C.J. Lee, Y. Zhang, H. Takao, Y. Murayama, Y. Qian, A fluid–structure interaction study using patient-specific ruptured and unruptured aneurysm: the effect of aneurysm morphology, hypertension and elasticity, J. Biomech. 46 (14) (2013) 2402–2410, https://doi.org/10.1016/j.jbiomech.2013.07.016.

[19] H. Meng, V.M. Tutino, J. Xiang, A. Siddiqui, High WSS or low WSS? Complex interactions of hemodynamics with intracranial aneurysm initiation, growth, and rupture: toward a unifying hypothesis, Am. J. Neuroradiol. 35 (7) (2014) 1254–1262, https://doi.org/10.3174/ajnr.A3558.

[20] F.H. Epstein, G.H. Gibbons, V.J. Dzau, The emerging concept of vascular remodeling, N. Engl. J. Med. 330 (20) (1994) 1431–1438, https://doi.org/10.1056/NEJM199405193302008.
[21] A.M. Malek, Hemodynamic shear stress and its role in atherosclerosis, JAMA 282 (21) (1999) 2035, https://doi.org/10.1001/jama.282.21.2035.
[22] H.J. Steiger, Pathophysiology of development and rupture of cerebral aneurysms, Acta neurochirurgica. Supplementum 48 (1990) 1–57.
[23] J.R. Cebral, F. Mut, J. Weir, C. Putman, Quantitative characterization of the hemodynamic environment in ruptured and unruptured brain aneurysms, Am. J. Neuroradiol. 32 (1) (2011) 145–151, https://doi.org/10.3174/ajnr.A2419.
[24] A. Aranda, A. Valencia, Study on the relationship between wall shear stress and aspect ratio of cerebral aneurysms with different pressure differences using CFD simulations, J. Mech. Med. Biol. 18 (5) (2018) 1850055, https://doi.org/10.1142/S0219519418500550.
[25] M. Shojima, M. Oshima, K. Takagi, R. Torii, M. Hayakawa, K. Katada, T. Kirino, Magnitude and role of wall shear stress on cerebral aneurysm: computational fluid dynamic study of 20 middle cerebral artery aneurysms, Stroke 35 (11) (2004) 2500–2505, https://doi.org/10.1161/01.STR.0000144648.89172.0f.
[26] J.R. Cebral, M. Sheridan, C.M. Putman, Hemodynamics and bleb formation in intracranial aneurysms, Am. J. Neuroradiol. 31 (2) (2010) 304–310, https://doi.org/10.3174/ajnr.A1819.
[27] L. Jou, D.G. Britz, Correlation between aneurysm size and hemodynamics in one individual with multiple small intracranial aneurysms, Cureus (2016), https://doi.org/10.7759/cureus.683.
[28] J. Barahona, A. Valencia, M. Torres, Study of the hemodynamics effects of an isolated systolic hypertension (ISH) condition on cerebral aneurysms models, using FSI simulations, Appl. Sci. 11 (6) (2021) 2595, https://doi.org/10.3390/app11062595.
[29] Fatouraee, N., & Amini, A. A. (n.d.) Recovery of flow patterns in an abdominal aortic aneurysm phantom from phase contrast MRI. In Proceedings IEEE Workshop on Mathematical Methods in Biomedical Image Analysis. MMBIA-2000 (Cat. No. PR00737) (pp. 104–109). IEEE Comput. Soc. https://doi.org/10.1109/MMBIA.2000.852366.
[30] J.R. Cebral, F. Mut, D. Sforza, R. Löhner, E. Scrivano, P. Lylyk, C. Putman, Clinical application of image-based CFD for cerebral aneurysms, International Journal for Numerical Methods in Biomedical Engineering 27 (7) (2011) 977–992, https://doi.org/10.1002/cnm.1373.
[31] M.A.H. Mohd Adib, S. Ii, Y. Watanabe, S. Wada, Minimizing the blood velocity differences between phase-contrast magnetic resonance imaging and computational fluid dynamics simulation in cerebral arteries and aneurysms, Med. Biol. Eng. Comput. 55 (9) (2017) 1605–1619, https://doi.org/10.1007/s11517-017-1617-y.
[32] S. Omodaka, S. Sugiyama, T. Inoue, K. Funamoto, M. Fujimura, H. Shimizu, T. Tominaga, Local hemodynamics at the rupture point of cerebral aneurysms determined by computational fluid dynamics analysis, Cerebrovasc. Dis. 34 (2) (2012) 121–129, https://doi.org/10.1159/000339678.
[33] J. Xiang, S.K. Natarajan, M. Tremmel, D. Ma, J. Mocco, L.N. Hopkins, H. Meng, Hemodynamic–morphologic discriminants for intracranial aneurysm rupture, Stroke 42 (1) (2011) 144–152, https://doi.org/10.1161/STROKEAHA.110.592923.
[34] Y. Zhang, L. Jing, J. Liu, C. Li, J. Fan, S. Wang, X. Yang, Clinical, morphological, and hemodynamic independent characteristic factors for rupture of posterior communicating artery aneurysms, J. Neurointerventional Surg. 8 (8) (2016) 808–812, https://doi.org/10.1136/neurintsurg-2015-011865.
[35] H.T. Sun, K.Y. Sze, K.W. Chow, A.C. On Tsang, A comparative study on computational fluid dynamic, fluid-structure interaction and static structural analyses of cerebral aneurysm, Engineering Applications of Computational Fluid Mechanics 16 (1) (2022) 262–278, https://doi.org/10.1080/19942060.2021.2013322.
[36] R. Torii, M. Oshima, T. Kobayashi, K. Takagi, T.E. Tezduyar, Fluid–structure interaction modeling of a patient-specific cerebral aneurysm: influence of structural modeling, Comput. Mech. 43 (1) (2008) 151–159, https://doi.org/10.1007/s00466-008-0325-8.
[37] X. Ren, H. Li, K. Xu, Z. Li, B. Gao, W. Lu, T. Chen, Hemodynamic study on the therapeutic effects of varying diameter embolic coils in the treatment of intracranial aneurysms, International Journal for Numerical Methods in Biomedical Engineering 40 (3) (2024), https://doi.org/10.1002/cnm.3807.
[38] M. Schena, F. Testa, M. Bozzetto, A. Remuzzi, L.A.A. Lanterna, E. Lanzarone, A CFD-based framework to evaluate surgical alternatives in cerebral aneurysms, Comput. Methods Biomech. Biomed. Eng.: Imaging & Visualization (2024) 1–13, https://doi.org/10.1080/21681163.2024.2325351.
[39] S. Ramalho, A. Moura, A.M. Gambaruto, A. Sequeira, Sensitivity to outflow boundary conditions and level of geometry description for a cerebral aneurysm, International Journal for Numerical Methods in Biomedical Engineering 28 (6–7) (2012) 697–713, https://doi.org/10.1002/cnm.2461.
[40] S. Makino, K. Shimano, S. Shiratori, H. Nagano, H. Ujiie, Influence of different outflow boundary conditions on hemodynamic analysis of cerebral aneurysm, Journal of Biorheology 37 (1) (2023) 21–34, https://doi.org/10.17106/jbr.37.21.
[41] H. Darvish, N. Fatouraee, M. Nabaei, Numerical investigation of perfusion rates in the circle of Willis in different anatomical variations and ischemic stroke, Phys. Fluids 33 (4) (2021) 041901, https://doi.org/10.1063/5.0040348.
[42] M.L. Raghavan, B. Ma, R.E. Harbaugh, Quantified aneurysm shape and rupture risk, J. Neurosurg. 102 (2) (2005) 355–362, https://doi.org/10.3171/jns.2005.102.2.0355.
[43] Ø. Evju, K.-A. Mardal, On the Assumption of Laminar Flow in Physiological Flows: Cerebral Aneurysms as an Illustrative Example (2015) 177–195, https://doi.org/10.1007/978-3-319-05230-4_7.
[44] M. Shojima, M. Oshima, K. Takagi, R. Torii, K. Nagata, I. Shirouzu, T. Kirino, Role of the bloodstream impacting force and the local pressure elevation in the rupture of cerebral aneurysms, Stroke 36 (9) (2005) 1933–1938, https://doi.org/10.1161/01.STR.0000177877.88925.06.
[45] Y. Zhang, X. Yang, Y. Wang, J. Liu, C. Li, L. Jing, H. Li, Influence of morphology and hemodynamic factors on rupture of multiple intracranial aneurysms: matched-pairs of ruptured-unruptured aneurysms located unilaterally on the anterior circulation, BMC Neurol. 14 (1) (2014) 253, https://doi.org/10.1186/s12883-014-0253-5.
[46] K. Fukazawa, F. Ishida, Y. Umeda, Y. Miura, S. Shimosaka, S. Matsushima, H. Suzuki, Using computational fluid dynamics analysis to characterize local hemodynamic features of middle cerebral artery aneurysm rupture points, World Neurosurgery 83 (1) (2015) 80–86, https://doi.org/10.1016/j.wneu.2013.02.012.
[47] J. Xu, Y. Yu, X. Wu, Y. Wu, C. Jiang, S. Wang, J. Liu, Morphological and hemodynamic analysis of mirror posterior communicating artery aneurysms, PLoS One 8 (1) (2013) e55413, https://doi.org/10.1371/journal.pone.0055413.
[48] G. Byrne, F. Mut, J. Cebral, Quantifying the large-scale hemodynamics of intracranial aneurysms, Am. J. Neuroradiol. 35 (2) (2014) 333–338, https://doi.org/10.3174/ajnr.A3678.
[49] M.R. Crompton, Mechanism of growth and rupture in cerebral berry aneurysms, BMJ 1 (5496) (1966) 1138–1142, https://doi.org/10.1136/bmj.1.5496.1138.